



Electron Acceleration by Moderate-Mach-number Low- β Shocks: Particle-in-Cell Simulations

Chunkai Yu¹ , Zhongwei Yang^{2,3} , Xinliang Gao⁴ , Quanming Lu⁴ , and Jian Zheng^{1,4,5,6}

¹ Department of Plasma Physics and Fusion Engineering, University of Science and Technology of China, Hefei, 230026, People's Republic of China
ckyu@mail.ustc.edu.cn

² State Key Laboratory of Space Weather, National Space Science Center, Chinese Academy of Sciences, Beijing, 100190, People's Republic of China
zwyang@swl.ac.cn

³ Key Laboratory of Polar Science, MNR, Polar Research Institute of China, Shanghai 200136, People's Republic of China

⁴ CAS Key Laboratory of Geospace Environment, Chinese Academy of Sciences, University of Science and Technology of China, Hefei, 230026, People's Republic of China

⁵ CAS Center for Excellence in Ultra-Intense Laser Science, Shanghai 201800, People's Republic of China

⁶ Collaborative Innovation Center of IFSA, Shanghai Jiao Tong University, Shanghai 200240, People's Republic of China

Received 2022 March 17; revised 2022 April 13; accepted 2022 April 14; published 2022 May 16

Abstract

Particle acceleration is ubiquitous at shock waves, occurring on scales ranging from supernova remnants in the universe to coronal-mass-ejection-driven shocks and planetary bow shocks in the heliosphere. The most promising mechanism responsible for the almost universally observed power-law spectra is diffusive shock acceleration (DSA). However, how electrons are preaccelerated by different shocks to the energy required by the DSA theory is still unclear. In this paper, we perform two-dimensional particle-in-cell plasma simulations to investigate how the magnetic field orientations, with respect to simulation planes, affect electron preacceleration in moderate-Mach-number low- β shocks. Simulation results show that instabilities can be different as the simulation planes capture different trajectories of particles. For magnetic fields perpendicular to the simulation plane, electron cyclotron drift instability dominates in the foot. Electrons can be trapped by the electrostatic wave and undergo shock-surfing acceleration. For magnetic fields lying in the simulation plane, whistler waves produced by modified two-stream instability dominate in the foot and scatter the electrons. In both cases, electrons undergo multistage acceleration in the foot, shock surface, and immediate downstream, during which process shock-surfing acceleration takes place as part of the preacceleration mechanism in moderate-Mach-number quasi-perpendicular shocks.

Unified Astronomy Thesaurus concepts: [Shocks \(2086\)](#); [Plasma astrophysics \(1261\)](#)

1. Introduction

Electron acceleration has attracted much attention in astrophysical, space, and laboratory plasma physics. Radio and X-ray observations of supernova remnant shocks suggest that there are relativistic electrons in front of the shocks (Koyama et al. 1995; Bamba et al. 2003). Diffusive shock acceleration (DSA) is believed to account for the acceleration (Krymskii 1977; Bell 1978; Drury 1983), and it naturally predicts a power-law energy spectrum that has a characteristic spectrum index close to the values derived from the observations. However, the DSA mechanism only works for particles whose Larmor radii are much larger than the shock width, assumed to be a few gyroradii of thermal ions. Given the small mass and small gyroradius of electrons, how they are accelerated to energies that can be injected into the DSA remains unsolved.

One possible candidate for the injection problem is shock surfing acceleration (SSA; Katsouleas & Dawson 1983; Shimada & Hoshino 2000; Hoshino & Shimada 2002), wherein electrons trapped by electrostatic waves in front of the shock undergo drift motion in the direction of the motional electric field. Hoshino et al. (Hoshino & Shimada 2002) studied electron SSA in perpendicular collisionless shocks using the 1D PIC method and found that electrons gained relativistic energy. Amano & Hoshino (2008) found that the efficient electron energization occurred at

the leading edge of the high-Mach-number shock transition region through the interactions with large-amplitude electrostatic waves produced by the Buneman instability. Bohdan et al. (2017) performed 2D PIC simulations to study electron injection and acceleration processes in perpendicular collisionless shocks with high Alfvénic Mach numbers and showed evidence that the efficiency of electron acceleration depends on the choice of the orientation of the large-scale magnetic field with respect to the simulation plane. In the high-Mach-number shocks, Buneman instability is excited as the bulk velocity of the reflected ions exceeds the thermal velocity of upstream electrons. In moderate- or low-Mach-number shocks, the condition for Buneman instability could not be satisfied. In moderate-Mach-number shocks, previous 1D (Muschiatti & Lembège 2006) and 2D (Yang et al. 2020a) simulations show that electron cyclotron harmonic (ECH) waves can play an important role in the electron trapping and acceleration process. Furthermore, the modulation of shock-front rippling (Johlander et al. 2016) and self-reformation (Yang et al. 2020b) on the electrostatic wave excitation is also presented by 2D PIC simulations (Yang et al. 2018). However, the effects of magnetic field orientations relative to the 2D simulation plane on the wave excitation and the electron energization at moderate-Mach-number shocks have not been parametrically investigated yet.

Limited by computational resources and motivated by the difference in the projections of electrons' motion with respect to simulation planes, we carry out 2D PIC simulations wherein the planes capture different parts of the electrons' trajectories. In our simulations, the magnetic field is perpendicular or



Original content from this work may be used under the terms of the [Creative Commons Attribution 4.0 licence](#). Any further distribution of this work must maintain attribution to the author(s) and the title of the work, journal citation and DOI.

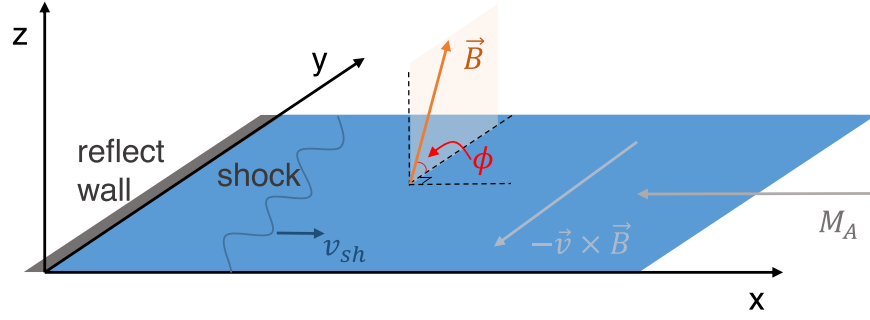


Figure 1. An illustration of the setup.

parallel to the simulation plane. In this way, we study how the orientations of magnetic fields with respect to simulation planes affect electron acceleration in perpendicular shocks.

This paper is organized as follows. We describe our simulation model for two cases: in-plane magnetic fields and out-of-plane magnetic fields in Section 2. In Section 3, we present our result that different waves appear in the foot regions, and an analysis of a typical electron is presented to study the physics of electron acceleration. Section 4 gives a summary and discussion.

2. Numerical Method

Simulations are performed in the x - y plane using the PIC code EPOCH (Arber et al. 2015; Yang et al. 2015, 2016). The upstream magnetization $\omega_{pe}/\omega_{ce} = 2.5$, where ω_{pe} and ω_{ce} are the plasma frequency and electron cyclotron frequency of upstream plasma. The ratio of the ion's mass to the electron's mass m_i/m_e is set to be 100. Simulations have the grids $[n_x, n_y] = [14,000, 2000]$. The spatial resolution is set to be $\Delta x = \Delta y = 0.005d_i$, where $d_i (=c/\omega_{pi})$ is the upstream ion inertial length. Each grid has 36 particles per species. We set the values of density and magnetic field to be $n_0 = B_0 = 1$ in the upstream, and the motional electric field is initialized with $\mathbf{E} = -\mathbf{v} \times \mathbf{B}$. Plasma beta, the ratio of thermal pressure to magnetic pressure, is set to be $\beta_i = \beta_e = 0.05$. Initially, the plasma has the bulk velocity u_0 along $-x$ with Alfvénic Mach $M_A = 8$, and the incident particles are reflected at the left reflective boundary (Figure 1). The shock is formed by the interaction of incoming upstream and reflected plasma and propagates in the $+x$ direction. In all cases, time and spatial ordinates are normalized by $1/\omega_{ci}$, and d_i , respectively, where ω_{ci} is the upstream ion cyclotron frequency.

The magnetic field lies in the y - z plane, and an angle ϕ is formed between the magnetic field and simulation plane. Here we show two cases to study the physics of different orientations between magnetic fields and simulation planes. Both are perpendicular shocks. We note "Case_A" for $\phi = 90^\circ$ and "Case_B" for $\phi = 0^\circ$.

3. Simulation Results

3.1. Case_A

In this case, $\phi = 90^\circ$, the magnetic field is oriented in the $+z$ direction. Figure 2 shows the shock profiles at $\omega_{ci}t = 5$. The foot region can be clearly distinguished between the overshoot at $x = 15c/\omega_{pi}$ and the unperturbed upstream at $x \geq 18c/\omega_{pi}$. In the downstream $x \leq 15c/\omega_{pi}$, the densities fluctuate around a constant value and reach the compression ratio $r = 2.2$. Note that magnetic field perturbations are along the initial magnetic

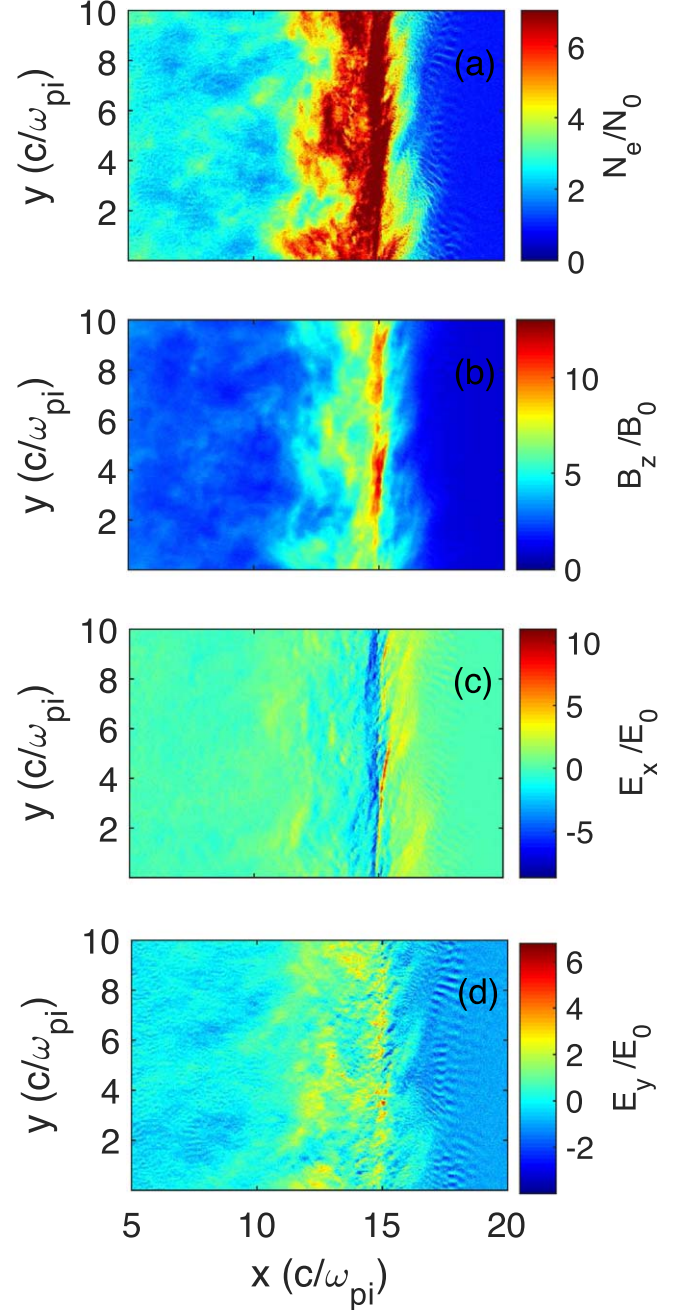


Figure 2. Shock profile at $\omega_{ci}t = 5$ for Case_A. (a) y -averaged electron and ion density. (b) The z -component magnetic field B_z normalized by the initial value. (c) The x -component electric field E_x normalized by the upstream motional electric field strength $E_0 = u_0 B_0$. (d) The y -component electric field E_y normalized by E_0 .

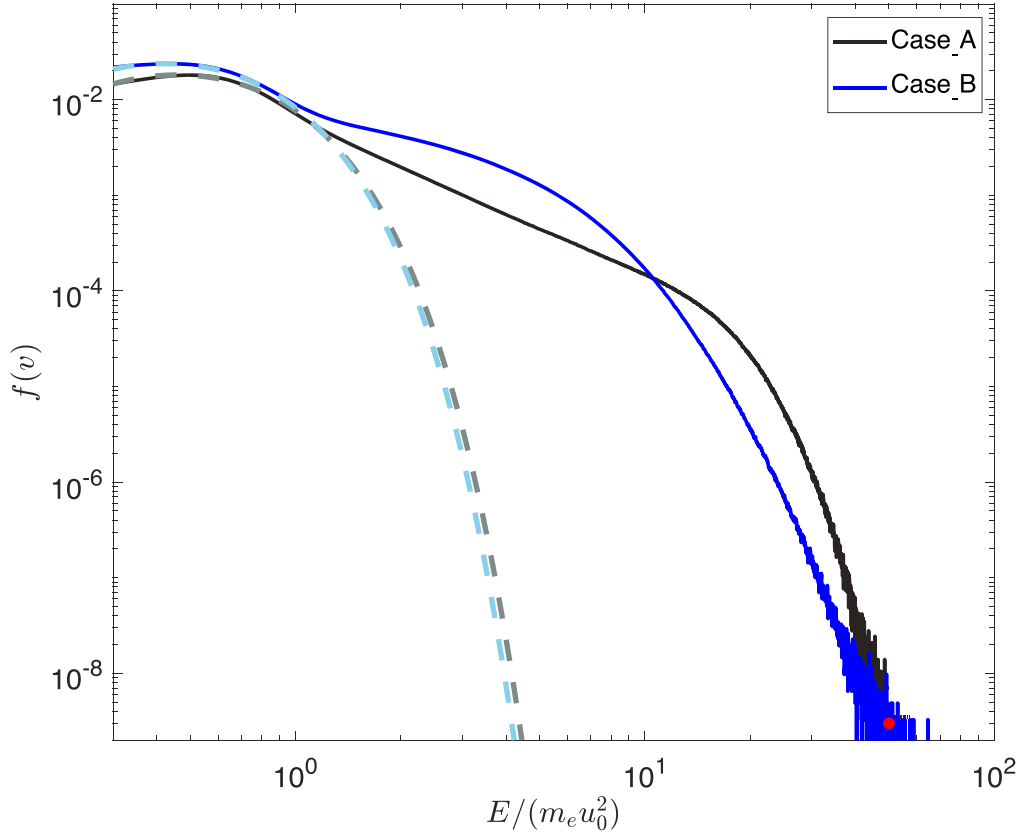


Figure 3. Electron spectra of foot regions $\omega_{ci}t = 5$ for Case_A and Case_B, as shown by the solid lines. The Maxwellian fit of Case_A is shown by the gray dashed line and the one corresponding to Case_B is shown by the light-blue dashed line. The red dot represents the electrons selected to be analyzed in Case_A and Case_B.

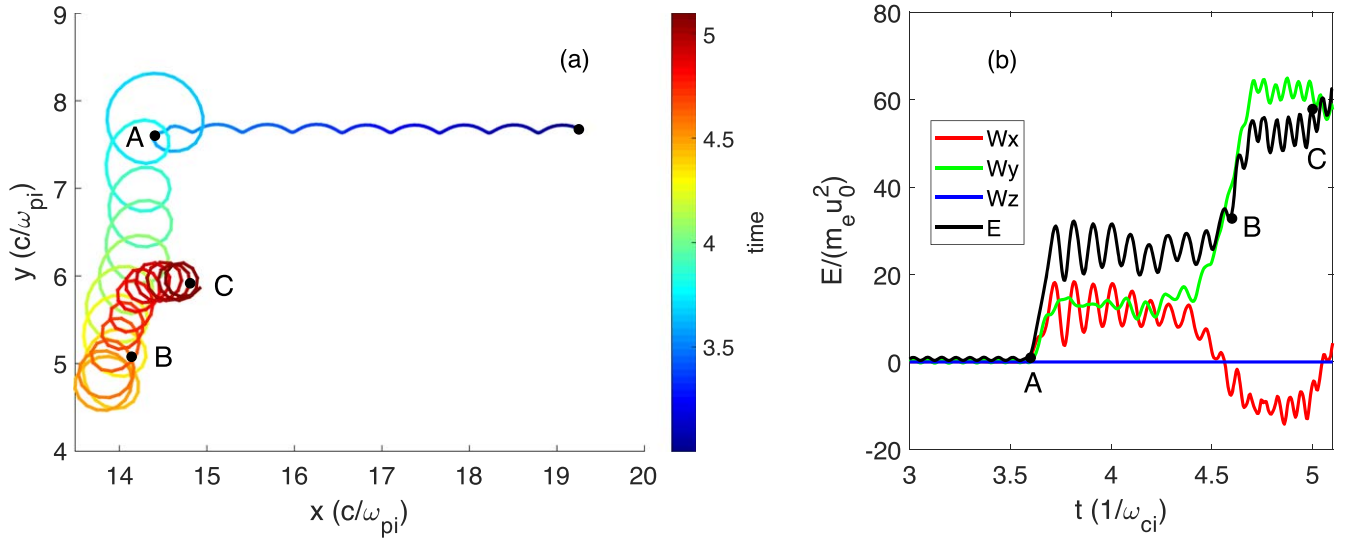


Figure 4. The typical electron's trajectory (a) and energy evolution (b) for Case_A. Three marked points, A, B, and C, represent three different stages in the electron's acceleration process: (A) encounter ECDI, (B) accelerating near the shock surface, and (C) trapped in the immediate downstream.

field, which indicates that the shock is perpendicular to the magnetic field everywhere. Electrostatic wave in the foot is observed in electric field profiles (Figures 2(c)–(d)). The wave is excited by electron cyclotron drift instability (ECDI), which is caused by the coupling of the electron Bernstein wave and the ion-beam mode (Yang et al. 2020b). The appearance of the ECDI plays an important role in electron acceleration.

Figure 3 shows the normalized electron spectrum at the foot region at $\omega_{ci}t = 5$ for Case_A and Case_B. The energy is normalized by the upstream kinetic energy $m_e u_0^2$. The maximal kinetic energy E_{\max} reaches $60m_e u_0^2$ for both cases, which is larger than its Maxwellian fit by an order, which is shown by the dashed lines. Accelerated electrons form the nonthermal part of the spectrum between $E \sim 20m_e u_0^2$ and $E \sim 50m_e u_0^2$.

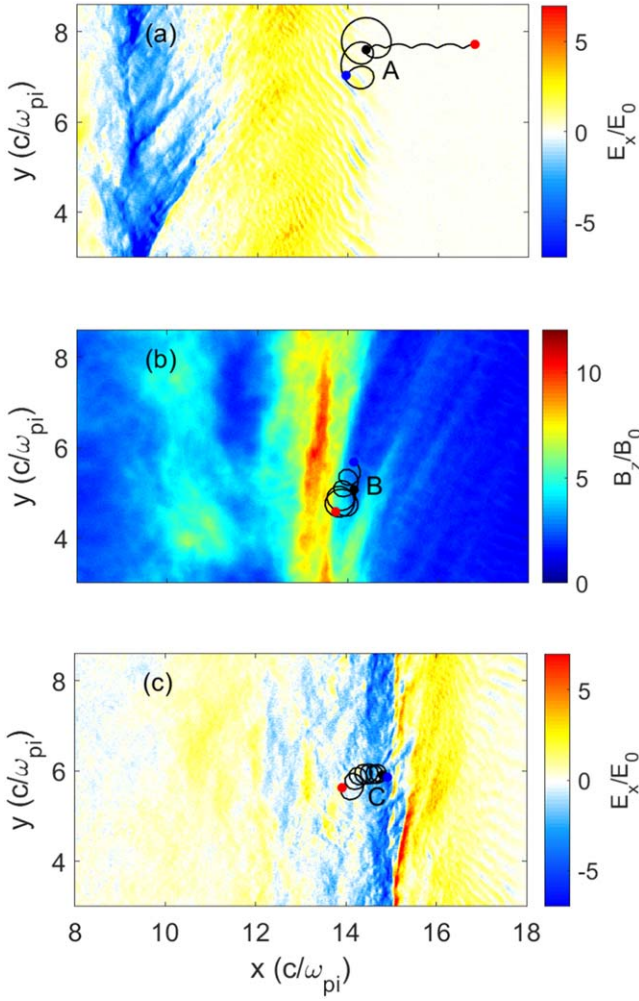


Figure 5. The electron’s trajectory and its position with respect to the shock for Case_A. (a)–(c): electric field $E_x(\omega_{ci}t = 3.6)$, magnetic field $B_z(\omega_{ci}t = 4.6)$, and electric field $E_x(\omega_{ci}t = 5.0)$. In each subplot, the start time of part of the trajectory is indicated by the red dot, whereas the blue dot denotes the end time of the part of the trajectory. The electron is located at the position indicated by the black dot at the same time as the snapshot of the field, also marked by A, B, and C. The start and end times of each subplot: (a) $\omega_{ci}t = 3.3$ – 3.9 , (b) $\omega_{ci}t = 4.4$ – 4.73 , and (c) $\omega_{ci}t = 4.74$ – 5.1 .

In order to study the physics of electron acceleration, we trace millions of electrons from the upstream to the shock fronts. One striking point is that the electrons forming the nonthermal part have similar trajectories and accelerated processes. A typical electron’s accelerated history is shown in Figure 4. In Figure 4(b), work done by the electric field along the i -axis is calculated as $W_i = \frac{e}{m_e} \int v_{e,i} E_i dt$, where $v_{e,i}$ and E_i represent the electron’s velocity and electric field along the axis, respectively. From the trajectory in Figure 4(a) and the energy evolution in Figure 4(b), acceleration in front of the shock can be divided into two stages: (1) encountering ECDI at $\omega_{ci}t = 3.6$ and (2) the subsequent process at the shock surface starting from $\omega_{ci}t = 4.4$.

Initially, the electron is located in the upstream and drifts along the x -axis, as indicated by the sinusoidal part of the trajectory between the starting point and point A in $x \geq 14.5c/\omega_{pi}$ in Figure 4(a). When the electron moves to position $x = 14.5c/\omega_{pi}$ at $\omega_{ci}t = 3.6$ —point A—the electron encounters the foot’s leading edge and is trapped by ECDI

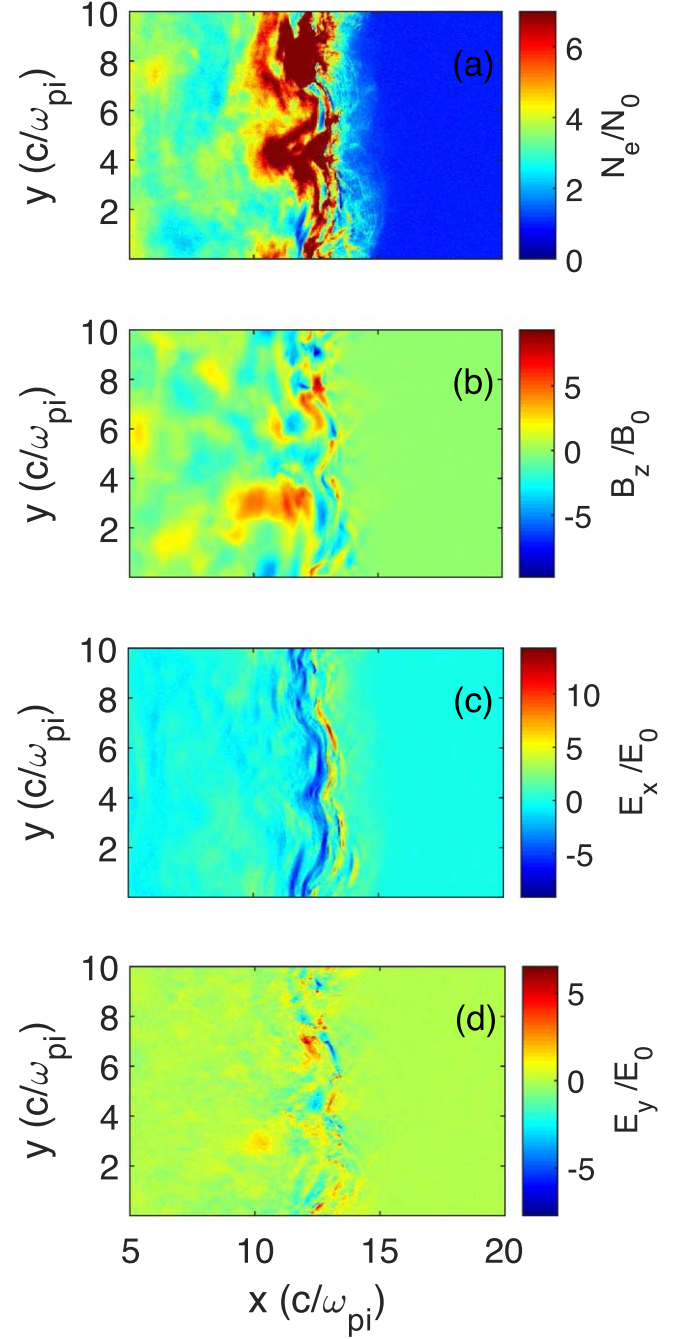


Figure 6. Shock profile at $\omega_{ci}t = 5$ for Case_B. (a) y -averaged electron and ion density. (b) The z -component of the magnetic field B_z normalized by the initial value. (c) x -component of the electric field E_x normalized by the upstream motional electric field strength E_0 . (d) y -component of the electric field E_y , normalized by E_0 .

(Figure 5(a)). Resonating with ECDI contributes to part of the first-stage energy gain. The trapping can also be demonstrated by the work done by E_x , represented by the red line starting from point A in Figure 4(b). Besides, there is also an energy gain from E_y , represented by the green solid line, resulting from SSA when the electron is trapped by ECDI. The electron’s gyroradius increases as the result of this first-stage acceleration and then it drifts along the y -axis as it approaches the shock ramp. The electron bounces along the x -axis and drifts along the y -axis with $v_y \sim -3v_A$, determined by $E_x \times B_z$ when encountering ECDI. The motional electric field E_y experienced

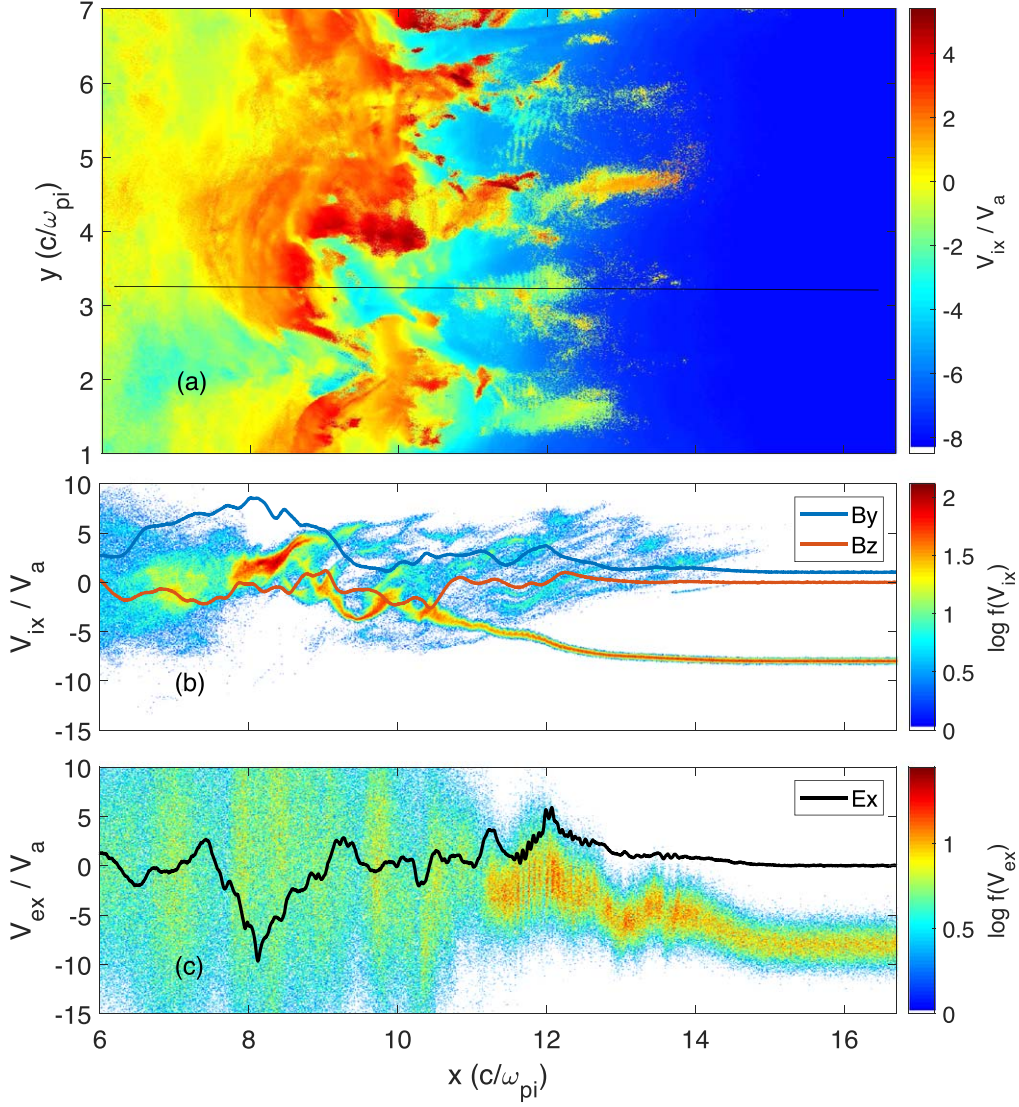


Figure 7. 2D MTSI in Case_B. (a) The ion's x -component velocity space distribution at $\omega_{ci}t = 4$. (b) The ion's x -component velocity phase diagram at $y = 4c/\omega_{pi}$, as indicated by the solid black line in (a), and the blue and brown lines indicate the y -component and z -component of the magnetic field B_y, B_z at the same region. (c) The electron's x -component velocity phase diagram at $y = 4c/\omega_{pi}$, and the black line indicates the component of the electric field E_x .

by the electron is nearly canceled out due to the strong electrostatic fluctuations around $x = 13.5 \sim 14.5c/\omega_{pi}$, which makes the work done by E_y unchanged in this interval. Figure 5(b) shows part of the electron's trajectory from $\omega_{ci}t = 4.4$ to $\omega_{ci}t = 4.73$ when the electron is near the shock ramp. The colored shock pattern is the normalized z -component magnetic field B_z . At the time, the shock is propagating at $x = 13c/\omega_{pi}$, as indicated by the position of the overshoot, shown in red. Ahead of the overshoot, there is a local maximal magnetic field around $x = 14c/\omega_{pi}$ and the structure is moving along the shock surface. This is the new shock surface as a result of shock self-reforming. The electron meets the new reforming shock surface when drifting along the shock surface and then is reflected into the $+y$ direction. In the later process, the electron gyrates around the shock ramp, the stage marked point B in Figure 4(a), and the energy gain is from the motional electric field E_y , as indicated by the green solid line in Figure 4(b) at $\omega_{ci}t = 4.4$. After leaving the shock ramp and advecting downstream, the electron is trapped in the region just behind the shock surface, the stage marked point C in

Figure 4(a). In the immediate downstream, motional electric field E_x is produced by plasma crossing the downstream magnetic field B_z when moving along the $-y$ direction. This electric field contributes to the slight energy increase at $\omega_{ci}t = 5$. In this acceleration process happening in the downstream, the electron moves along the $+x$ -axis while being trapped in the immediate downstream electric field as indicated by Figure 5(c), and the energy increase is due to the work done by E_x as shown in Figure 4(b).

As the magnetic field B_z is perpendicular to the simulation plane x - y , the electrons' gyration can be fully captured. ECDI is excited by the coupled electron Bernstein wave and ion-beam mode. The electrostatic wave dominates the foot region, which is different from the Buneman instability that occurs in high-Mach-number shocks. ECDI affects the electron acceleration by capturing the electron, and the electron undergoes SSA at the same time. When approaching the shock surface, the electron drifts along the shock surface. After crossing the shock surface, the electron is trapped in the immediate downstream and moves along the shock-propagation direction.

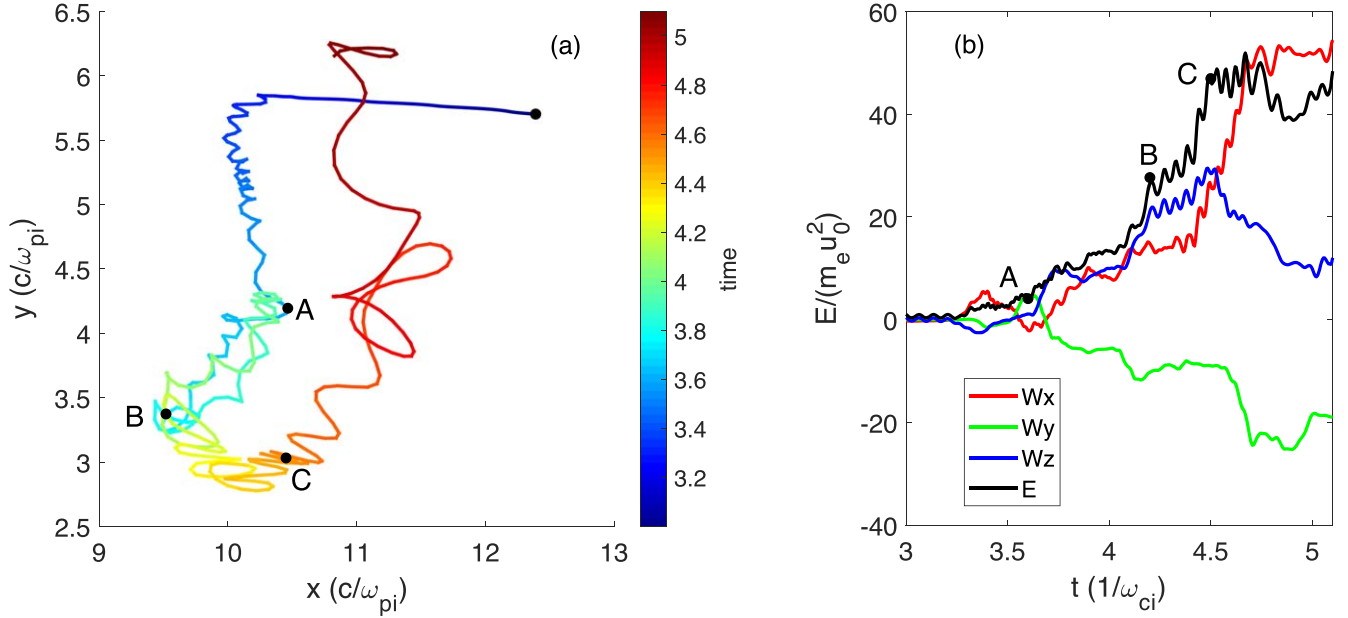


Figure 8. The typical electron’s trajectory (a) and energy evolution (b) for Case_B. The three marked points, A, B, and C, represent three different stages in the electron’s acceleration process: (A) scattered by the whistler wave, (B) SSA near the shock surface, and (C) trapped in the immediate downstream.

3.2. Case_B

Figure 6 shows the shock profile for $\psi = 0$ at $\omega_{ci}t = 5$. In this case, the magnetic field \mathbf{B} lies in the simulation plane and is oriented in the $+y$ -axis. At the time, the shock is propagating at about $x = 12.5c/\omega_{pi}$. The incoming plasma is compressed in the downstream, as shown by $x < 10c/\omega_{pi}$ (Figure 6(a)), and the compression ratio r reaches $r = 3$. In the foot region $13c/\omega_{pi} < x < 16c/\omega_{pi}$, there is an electromagnetic wave that can be seen in the magnetic fields (Figure 6(b)) and electric fields (Figure 6(c)–d). This is the whistler wave produced by the modified two-stream instability (MTSI), resulting from reflected unmagnetized ions drifting relative to incoming magnetized electrons across the homogeneous magnetic field. Figure 7(a) shows the x -component velocity space distribution at $\omega_{ci}t = 4$. At the time, the shock is propagating at $x = 9c/\omega_{pi}$, and perturbations can be clearly seen in the foot region, specifically in the regions $x \sim 12c/\omega_{pi}$, $y \sim 2c/\omega_{pi}$, $3.2c/\omega_{pi}$, and $5.4c/\omega_{pi}$. We choose one of the regions to analyze the MTSI, as indicated by the black line at $y = 3.2c/\omega_{pi}$. Figure 7(b) gives the ion’s x -component velocity phase diagram at the locations of the black line, whereas the corresponding electron’s x -component velocity phase diagram is shown in Figure 7(c). Perturbation on incoming ions at $x = 11 - 12c/\omega_{pi}$ matches the perturbation on the electron. The blue and brown lines in Figure 7(b) and the black line in Figure 7(c) are B_y , B_z , and E_x at $y = 3.2c/\omega_{pi}$. MTSI has been widely investigated in previous works (Wu et al. 1983; Matsukiyo & Scholer 2003; Scholer et al. 2003; Scholer & Burgess 2007) by using the 1D PIC method. However, no work has reported that MTSI exists in 2D simulations. In our 2D PIC simulations, we find that MTSI does exist as shown in Figure 7, and a quasi-perpendicular shock may be formed locally thanks to the presence of ripples.

The whistler wave in the foot region can significantly affect the electrons’ acceleration process. As shown in Figure 3, the spectrum of the foot-region electrons with respect to their kinetic energy is depicted by the blue solid line, whose maximal kinetic energy reaches $E_{\max} = 60m_e u_0^2$. To investigate

the physics of the acceleration of nonthermal electrons in this case, we trace electrons from the upstream initially and collect the work done by the electric fields, respectively. Figure 8 gives the trajectory and energy evolution of a typical electron. According to the kinetic energy, acceleration of the particle can be divided into three stages: scattered by the whistler wave, SSA, and trapped in the immediate downstream.

Initially, the electron’s trajectory is straight at $10.5c/\omega_{pi} < x < 12.5c/\omega_{pi}$ as it drifts from the upstream to the foot, not like the sinusoidal curve shown in Figure 5(a). This is the result of different choices of the angle ϕ . When $\phi = 90^\circ$, the whole electron’s gyromotion $R(x, y)$ is captured by the simulation plane x – y in Figure 5(a), whereas in the case where $\phi = 0^\circ$, only the projection of the electron’s gyromotion $R(x, z)$ can be captured by the simulation plane, which is shown by a straight line Figure 9(a). From $\omega_{ci}t = 3.4$ onward, the electron moves into the foot and is scattered by the whistler wave, the stage marked point A (Figure 8(a)), which results in the electron moving along the shock surface Figure 9(a). The scattering by the whistler wave is vital for the subsequent acceleration process as the electrons that are not scattered by the whistler wave will penetrate the shock directly and have little energy gain. As it approaches the shock ramp at $\omega_{ci}t = 4$, the electron goes through the SSA process. In this stage, the electron runs into a unipolar electric field as indicated by the arrows in Figure 9(b). The work done by the motional electric field E_z contributes to the total energy gain, as shown by the point marked B in Figure 8(b) at $4 < \omega_{ci}t < 4.4$. After the SSA process, the electron crosses the shock and is captured in the immediate downstream region, where the electron meets the motional electric field E_x . This results in the third-stage acceleration where the work done by E_x contributes to the total energy gain, as indicated by the red line at $\omega_{ci}t \sim 4.5$, marked as C, in Figure 8(b).

In this case, the magnetic field B_y lies in the simulation plane x – y , and only part of the electrons’ gyration can be captured. The whistler wave dominates the foot region as a result of MTSI. The electrons can be scattered by the whistler wave,

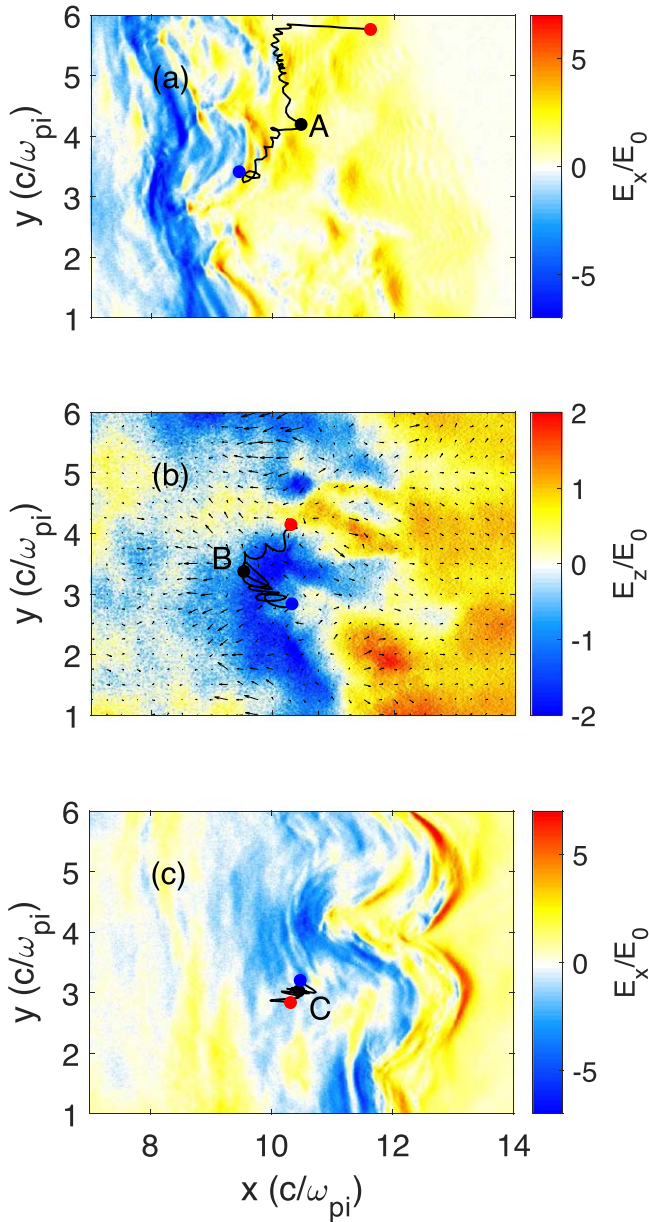


Figure 9. The electron's trajectory and its position with respect to the shock for Case_B. (a)–(c): electric field E_x ($\omega_{cift} = 3.6$), electric field E_z ($\omega_{cift} = 4.2$), and electric field E_x ($\omega_{cift} = 4.5$). The start and end times of each subplot: (a) $\omega_{cift} = 3.1$ –3.8, (b) $\omega_{cift} = 4$ –4.4, and (c) $\omega_{cift} = 4.4$ –4.6. The arrows in (b) indicate the direction and strength of the vector (E_x , E_y).

decelerating the electrons in the shock-propagation direction. When approaching the shock surface, the electrons go through SSA. The electrons could be trapped in the immediate downstream after crossing the shock surface.

4. Summary and Discussion

We study how the orientations of magnetic fields with respect to simulation planes affect electron acceleration in perpendicular shocks. In the two cases where $\phi = 90^\circ$, where the magnetic field is perpendicular to the simulation plane, and $\phi = 0^\circ$, where the magnetic field is lying in the simulation plane, different waves are produced in the foot because of the difference in the gyromotion of particles captured by the simulation plane. In the case where $\phi = 90^\circ$, ECDI is excited

by the coupling of the electron Bernstein wave and reflected ion-beam mode, whereas the whistler wave is produced by the 2D MTSI in the case where $\phi = 0^\circ$. The interactions of electrons and foot-region waves are also quite different in the two cases. In the case where $\phi = 90^\circ$, the electrons that form a nonthermal component experience resonance with ECDI and SSA processes at the foot's leading edge, and then the electrons go through the shock drift acceleration (SDA) process when they are around the shock ramp. In the case where $\phi = 0^\circ$, the electrons are scattered by the whistler wave in the foot and then go through SSA around the shock ramp. In both cases, the electrons are trapped by the immediate downstream motional electric field along the x -axis and would finally advect downstream.

Our work shows different electron acceleration mechanisms can be operated when different simulation planes are chosen. In both cases, electrons can be efficiently accelerated to form nonthermal parts of the distributions. This work is helpful for understanding the injection problem that is an unsolved question in DSA theory.

We thank the team of developers and maintainers of EPOCH. And this work is supported by the Strategic Priority Research Program of Chinese Academy of Sciences (grant No. XDA25010200), the NSFC Grants (41574140, 42150105), National Key R&D Program of China (No. 2021YFA0718600), the project of Civil Aerospace “13th Five Year Plan” Preliminary Research in Space Science (Nos. D020301 and D030202), the Specialized Research Fund for State Key Laboratories of China, and the Open Research Program Key laboratory of Polar Science, MNR (KP202005). Q. L. acknowledges partial support by the Strategic Priority Research Program of CAS (XDB 41000000).

ORCID iDs

Chunkai Yu <https://orcid.org/0000-0002-3478-9180>
 Zhongwei Yang <https://orcid.org/0000-0002-1509-1529>
 Xinliang Gao <https://orcid.org/0000-0003-0767-2267>
 Quanming Lu <https://orcid.org/0000-0003-3041-2682>

References

- Amano, T., & Hoshino, M. 2008, *ApJ*, **690**, 244
 Arber, T. D., Bennett, K., Brady, C. S., et al. 2015, *PPCF*, **57**, 113001
 Bamba, A., Yamazaki, R., Ueno, M., & Koyama, K. 2003, *ApJ*, **589**, 827
 Bell, A. R. 1978, *MNRAS*, **182**, 147
 Bohdan, A., Niemiec, J., Kobzar, O., & Pohl, M. 2017, *ApJ*, **847**, 71
 Drury, L. O. 1983, *RPPH*, **46**, 973
 Hoshino, M., & Shimada, N. 2002, *ApJ*, **572**, 880
 Johlander, A., Vaivads, A., Khotyaintsev, Y. V., Retinò, A., & Dandouras, I. 2016, *ApJL*, **817**, L4
 Katsouleas, T., & Dawson, J. M. 1983, *PhRvL*, **51**, 392
 Koyama, K., Petre, R., Gotthelf, E. V., et al. 1995, *Natur*, **378**, 255
 Krymskii, G. F. 1977, *SPhD*, **22**, 327
 Matsukiyo, S., & Scholer, M. 2003, *JGRA*, **108**, 1459
 Muschietti, L., & Lembège, B. 2006, *AdSpR*, **37**, 483
 Scholer, M., & Burgess, D. 2007, *PhPI*, **14**, 072103
 Scholer, M., Shinohara, I., & Matsukiyo, S. 2003, *JGRA*, **108**, 4
 Shimada, N., & Hoshino, M. 2000, *ApJL*, **543**, L67
 Wu, C. S., Winske, D., Papadopoulos, K., et al. 1983, *PhFI*, **26**, 1259
 Yang, Z., Huang, C., Liu, Y. D., et al. 2016, *ApJS*, **225**, 13
 Yang, Z., Liu, Y. D., Matsukiyo, S., et al. 2020b, *ApJL*, **900**, L24
 Yang, Z., Liu, Y. D., Richardson, J. D., et al. 2015, *ApJ*, **809**, 28
 Yang, Z., Liu, Y., Johlander, A., et al. 2020a, *ApJL*, **901**, L6
 Yang, Z., Lu, Q., Liu, Y. D., & Wang, R. 2018, *ApJ*, **857**, 36